Environmental Science
Water Research & Technology

Phosphate-binding protein-loaded iron oxide particles: Adsorption performance for phosphorus removal and recovery from water

Journal:	*Environmental Science: Water Research & Technology*
Manuscript ID	EW-ART-01-2024-000052.R1
Article Type:	Paper

Water Impact Statement

Immobilized phosphate-binding proteins (PBPs) offer highly selective, reversible phosphorus adsorption, which can help address nutrient pollution while enabling a circular phosphorus economy. Increasing the adsorption capacity of PBP adsorbents is critical for implementation and should proceed with parallel increases in the surface area to mass ratio of the immobilization matrix and reductions in the size of the phosphorus-selective binding sequence.

Phosphate-binding protein-loaded iron oxide particles: Adsorption performance for phosphorus removal and recovery from water

Faten B. Hussein[1], Andrew H. Cannon[2], Justin M. Hutchison[3], Christopher B. Gorman[4], Yaroslava G. Yingling[2], Brooke K. Mayer[1*]

[1] Department of Civil, Construction and Environmental Engineering, Marquette University, 1637 West Wisconsin Avenue, Milwaukee, WI, 53233, USA

[2] Department of Materials Science and Engineering, North Carolina State University, 911 Partners Way, Raleigh, NC, 27695, USA

[3] Department Civil, Environmental & Architectural Engineering, University of Kansas, 1530 W. 15th St., Lawrence, KS, 66045, USA

[4] Department of Chemistry, North Carolina State University, Box 8204, Raleigh, NC, 27695, USA

Emails:

Faten Hussein: faten.hussein@marquette.edu

Andrew Cannon: ahcannon@ncsu.edu

Justin Hutchison: jhutch@ku.edu

Christopher Gorman: cbgorman@ncsu.edu

Yaroslava G. Yingling: yara_yingling@ncsu.edu

*Corresponding author email: brooke.mayer@marquette.edu and phone: 414-288-2161

Abstract

Adsorbents featuring high-affinity phosphate-binding proteins (PBPs) have demonstrated highly selective and rapid phosphorus removal and recovery. While immobilized PBP is promising for inorganic phosphate (orthophosphate, P_i) removal and recovery, increased adsorption capacity of PBP-based materials is essential to enhance the feasibility of PBP for scaled implementation. Here, magnetic n-hydroxy succinimide (NHS)-activated iron oxide particles (IOPs) were used to immobilize PBP (PBP-IOPs). The PBP-IOPs provided rapid P_i removal, with more than 95% adsorption within 5 min. Slightly acidic pH (6), room temperature (20 ℃), and low ionic strength (0.01 M KCl) demonstrated the best removal efficiency. The P_i adsorption capacity of PBP-IOPs was not affected by anions such as chloride, sulfate, nitrate, bicarbonate, and borate. PBP-IOPs released 99% of total adsorbed P_i using pH adjustment. Conjugation of PBP to higher surface area per mass IOPs increased P_i attachment capacity (0.044 mg g^{-1}) relative to previous studies of PBP immobilized on Sepharose resin (0.0062 mg g^{-1}). Accordingly, PBP-IOPs have the potential to rapidly, spontaneously, selectively, and reversibly capture P_i. Theoretical capacity calculations indicated that parallel improvements in surface area to mass ratio of the base immobilization material together with reducing the size of the P_i-binding amino acid sequence (while retaining P_i specificity) are needed to further advance design and implementation of PBP-based adsorbents.

Keywords: Capacity, Desorption, Immobilization, Isotherm, Nutrient, Selectivity, Wastewater

1 Introduction

Inorganic phosphorous (predominantly orthophosphate, P_i) is critical for plant growth, but phosphate rock is a finite resource that is being continuously depleted to supply fertilizers for food production (1). Furthermore, release of excess P_i from anthropogenic sources (e.g., point sources

such as water resource recovery facilities as well as non-point sources such as agricultural runoff) contributes to eutrophic conditions in receiving waterbodies. It is therefore important to effectively *remove* and *recover* P_i from waste streams to better manage the anthropogenic P_i cycle. Chemical and biological technologies have been applied to remove P_i from different water matrices (2–4). However, some technologies such as biological processes struggle to meet increasingly low discharge standards of < 0.1 mg L^{-1} (5). Chemical precipitation, which can be used to remove P_i from high volume biologically treated effluent, has secondary issues (e.g., the process produces large amounts of chemical sludge, requiring clarification and disposal processes that add to the expense) (6).

Adsorption is a favorable approach to remove P_i by partitioning it to surfaces such that the P_i can be attached and then released under controlled conditions (7). Adsorption can provide a highly selective, low-cost approach for P_i removal and recovery (8). Adsorbent materials exhibit variable adsorptive selectivity and capacity, depending on the surface chemistry, porosity, and contact surface area (9). A common challenge for many adsorbents is selectivity given that target adsorbate removal can be significantly reduced through competition for adsorbent active sites by other competing ions (7). For instance, P_i removal from wastewater by iron oxide nanoparticles is affected by sulfate, chloride, and bicarbonate due to anion competition (10). Highly selective P_i adsorbents are therefore of great interest for improved removal performance and recovery of higher purity (higher value) phosphorus products.

Selective adsorption and desorption of P_i has been documented using several different configurations of immobilized high-affinity phosphate-binding proteins (PBP) (11–19). The mechanisms of P_i removal by PBP can be explored through molecular dynamics (MD) simulations within an industrial context. For example, MD simulations were used to explore the potential for

reagent-less biosensors by combining PBP with rhodamines, which emit fluorescence signals when the PBP is in its unbound conformation (20). Additionally, MD was used to study the effects of buffer solution on PBP binding affinities for different species of P_i, where PBP had a higher affinity for HPO_4^{2-} compared to $H_2PO_4^-$ (21). Interestingly, experimental data have shown a similar affinity between the two, possibly due to competition of buffer solutions with HPO_4^{2-}. The use of simulations can also elucidate the adsorption pathways and binding free energy profiles of PBP. Rigid-body Brownian dynamics simulations revealed that the *Escherichia coli* PBP possesses two distinct regions that attract anions and serve as screens for phosphates (22). Overall, MD simulations offer a powerful tool for gaining a deeper understanding of complex molecular interactions during P_i binding events.

Effective P_i removal to ultra-low levels (<100 μg L^{-1}) has been confirmed using immobilized PBPs (14,17,18). PBP adsorbents offer P_i release and recovery by adjusting solution pH to greater than 10, which yields a concentrated P_i solution that is suitable for reuse, e.g., as fertilizer feedstock (13). PBP provides improved adsorption in comparison to metal oxide adsorbents, offering at least 30 times faster adsorption, and at least 15 times higher affinity (17). Accordingly, immobilized PBP is a promising adsorbent material for P_i removal and recovery, and no improvements are needed in terms of affinity (17) or equilibrium (23). However, previous PBP research identified the need to enhance the material's adsorption capacity to make PBP a viable alternative for implementation (12,14,17,18).

To increase adsorbent capacity, particles with higher surface area to mass ratios may be used as the base material on which to immobilize PBP, e.g., micro- to nano-scale particles. A range of surfaces can be utilized for biomaterial conjugation (e.g., metals, polymers, or silica). Magnetic particles are attractive as they can be easily collected from environmental matrices using an

external magnetic field. Magnetic particles of variable composition and size have been extensively used in biomedical applications, such as drug delivery and enzyme conjugation, due to their unique properties such as stability, high surface area, and biocompatibility (24). Another application of magnetic particles is environmental remediation, for example, treating polluted water (25). Magnetic particles modified with functional groups (-NH_2, -COOH, -SH) and inorganic/organic-coated magnetic particles were used to adsorb heavy metals and toxic dyes (25).

In this study, magnetic NHS-activated iron oxide particles (IOPs) were used as the base material on which to immobilize PBP (i.e., PBP-IOPs). Although PBP has been studied for P_i binding and recovery, this is the first study to immobilize PBP on magnetic particles. The hypothesis was that the use of IOPs would increase the PBP loading capacity normalized to mass of adsorbent due to the smaller particle diameter (and hence, higher surface area to mass ratio) and increased ligand binding sites of IOPs, in turn increasing P_i adsorption capacity compared to previously established PBP-modified Sepharose resin (as reported by Venkiteshwaran et al., 2018) (18). It was also anticipated that PBP-IOPs would facilitate P_i recovery compared to unmodified IOPs because free P_i can be released from PBP binding sites by increasing solution pH, whereas P_i release from IOP-P complexes may be more difficult. The specific research objectives were to:

(1) Examine P_i adsorption kinetics using PBP-IOPs.

(2) Evaluate the effect of pH, temperature, and ionic strength (all of which often impact water/wastewater treatment process performance) on P_i removal efficiency.

(3) Evaluate the selectivity of the PBP-IOPs using Milli-Q water augmented with potentially competitive ions as well as tertiary wastewater effluent.

(4) Test the reusability of PBP-IOPs and compare performance to IOPs without conjugated PBP.

(5) Conduct isotherm modeling using the PBP-IOPs and assess its adsorption capacity compared to previous PBP adsorbent research.

(6) Calculate the theoretical maximum P_i binding capacity using PBP-IOPs vs. PBP immobilized on NHS-activated Sepharose resin to probe the materials' theoretical performance relative to actual experimental performance.

(7) Understand PBP and P_i interactions to determine the critical amino acids using molecular dynamics simulations.

2 Materials and Methods

2.1 Preparation of the PBP-IOP Adsorbent

The PBP-IOP adsorbent was prepared by immobilizing a purified solution of PBP onto BcMag^{TM} NHS-activated magnetic IOPs (Bioclone Inc, USA). A transmission electron microscopy image of the BcMag^{TM} NHS-activated magnetic IOPs showing the silica shell coating around the iron oxide core is included in the Supporting Information (SI). Preliminary control tests showed that the NHS-activated IOPs provided negligible P_i removal in the absence of PBP loading.

The PBP expression and purification procedures were conducted as described by Hussein and Mayer (2022) (14). Briefly, *E. coli* BL21 (DE3) competent cells containing the His-tagged *pstS* gene plasmid pET22b (#78198, Addgene, USA) were grown in Luria Broth (LB) with 100 μg mL^{-1} ampicillin at 37 ℃ with agitation at 250 rpm. When the cell suspension reached an OD_{600} value of 0.6-0.8, 1 mM isopropyl β-D-1-thiogalactopyranoside (IPTG) was added to induce PBP expression for 3-4 hr. PBP expression was confirmed by sodium dodecyl sulfate polyacrylamide gel electrophoresis (SDS-PAGE), as described by Hussein et al. (2020) (13). The induced cells were centrifuged for 20 min at 1250 ×g, and the cell pellets were collected for the purification step.

To purify PBP, the cell pellets were resuspended in 100 mL of binding buffer (50 mM NaH_2PO_4, 0.5 M NaCl, pH 8.0) and sonicated to rupture the cell membrane and release the cytoplasmic content. A Q500 sonicator (Qsonica, USA) was set at amplitude = 45%, pulse rate = 15 sec on and 45 sec off and 48 cycles of sonication were performed on ice. Supernatant from the cell's lysate was added to a Ni Sepharose™ 6 Fast Flow resin column (GE Healthcare Life Sciences, USA) to bind PBP for 60 min at room temperature. To release PBP from the column, an elution buffer (50 mM NaH_2PO_4, 0.5 M NaCl, 250 mM imidazole, pH 8.0) was used, and 5 mL eluted fractions were collected. The collected PBP fractions were combined and dialyzed in buffer (0.1 M $NaHCO_3$, 0.15 M NaCl, pH 7.4) using a Spectra/Por® 2 dialysis membrane (MWCO 12-14 kDa, Spectrum Laboratories, Inc., USA) at room temperature. The PBP concentration was measured using a Pierce™ BCA protein assay kit (Thermo Fisher Scientific, USA) and the dialyzed solution was stored in 14% glycerol at -80 ℃ until use.

The PBP was conjugated on the surface of BcMag™ NHS-activated magnetic IOPs (1 μm diameter) following the manufacturer's protocol with slight modification (pre-coupling wash step with deionized water instead of Tris buffer and blocking with Tris buffer instead of ethanolamine). The PBP solution (10 mL at 1 mg mL^{-1}) was added to 500 mg IOPs and mixed by gentle vortexing. The reaction tube was kept at room temperature for 4-6 hr with continuous mixing using a multi-purpose tube rotator (Fisherbrand™, Model No. 88861049). A magnetic bar was used to separate the PBP-IOPs from the PBP suspension. The supernatant was collected and the concentration of unbound PBP was measured using a Pierce™ BCA protein assay kit. The PBP coupling density was calculated as the amount of PBP attached (the difference in the PBP concentration in solution before and after attachment) multiplied by the volume of PBP solution and divided by the mass of IOPs. The PBP coupling density on the BcMag™ NHS-activated magnetic beads was 12-15 mg

PBP per g IOPs (0.343-0.429 μmole PBP per g IOPs), which compares favorably with the manufacturer-stated capacity of 1-20 mg protein per g IOP. The PBP-IOPs were resuspended in 10 mL blocking buffer (0.05 M Tris-HCl, 0.5 M NaCl, pH 8) at room temperature for 60 min. The PBP-IOPs were then washed with washing buffer (0.01 M Tris-HCl, 1 mM $MgCl_2$, pH 7) 2-3 times. The PBP-IOP adsorbent was stored at 4°C and used within 48 hr. To remove the legacy P_i adsorbed on PBP during the expression and purification processes, PBP-IOPs were washed with Tris buffer at pH 11.5-12 prior to adsorption experiments, which was previously reported to completely desorb P_i from PBP (18).

2.2 Phosphate Adsorption Kinetics

To examine P_i adsorption kinetics, 20 mg PBP-IOPs suspended in Tris buffer were gently vortexed and then added to a 2-mL microcentrifuge tube with 1 mg PO_4^{3-} L^{-1} (prepared in Tris-HCl buffer at pH 7). The 1-mL samples were mixed at 30 rpm using a multi-purpose tube rotator at room temperature for 1, 5, 10, 20, or 40 min. Triplicate tests were conducted at each reaction time. The P_i concentrations before and after adsorption were measured using the standard ascorbic acid method (26). The data was used to calculate the adsorption capacity by applying a mass balance relationship (Equation 1), as described by Wu et al. (2020) (27).

$$q_t = \frac{(C_0 - C_t)V}{m} \qquad \text{(Eq 1)}$$

where q_t is the amount of phosphate (mg g^{-1}) adsorbed at time (t), C_t is the phosphate concentration in solution (mg L^{-1}) at time (t), C_0 is the initial phosphate concentration (mg L^{-1}), V is the sample volume (mL), and m is the mass of adsorbent (mg).

Pseudo first-order (Equation 2) and pseudo second-order (Equation 3) kinetic models were used to model the data.

$$q_t = q_e (1 - e^{-k_1 t}) \qquad \text{(Eq 2)}$$

$$q_t = \frac{k_2 q_e^2 t}{1 + k^2 q_e t} \qquad \text{(Eq 3)}$$

where q_t is the amount of phosphate (mg g^{-1}) adsorbed at time (t), q_e is the amount of phosphate (mg g^{-1}) adsorbed at equilibrium, and k_1 (min^{-1}) and k_2 (g $mg^{-1}min^{-1}$) represent the first and second-order kinetic rate constants, respectively.

2.3 Effect of pH, Temperature, and Ionic Strength

Batch experiments were conducted to determine the effect of temperature, pH, and ionic strength on P_i adsorption. The baseline test conditions were pH 7, 20 ℃, and phosphate solution in Tris buffer (with no KCl addition). To evaluate the effect of pH on P_i adsorption, 1.1 mg PO_4^{3-} L^{-1} solution was prepared in Tris buffer at pH 4, 6, 7, 8, or 10. For temperature experiments, 1.1 mg PO_4^{3-} L^{-1} solution was prepared in Tris buffer at pH 7 which was equilibrated at 10, 20, 30, or 40 ℃ prior to the experiment. To study the effect of ionic strength on P_i adsorption, reaction buffers with 0.01, 0.05, 0.1, or 0.5 M KCl were mixed with 1 mg PO_4^{3-} L^{-1}.

For each experiment, 20 mg PBP-IOPs were used, and the suspensions were mixed at 30 rpm using a multi-purpose tube rotator. After 60 min, the reaction solution was separated from the PBP-IOPs using a magnetic bar and then analyzed for P_i.

2.4 Selectivity of PBP-IOPs

To test the selectivity of the PBP-IOPs, parallel experiments using 20 mg PBP-IOPs were conducted using multi-ion solution and P_i-only solution prepared in Milli-Q water (pH = 7). The multi-ion solution contained a final concentration of 1 mg L^{-1} each of NaCl, Na_2SO_4, $NaNO_3$, $NaHCO_3$, $B_4Na_2O_7 \cdot 10H_2O$, and KH_2PO_4. The associated anions are common competitors for P_i in wastewater. The P_i-only solution contained 1 mg L^{-1} KH_2PO_4. Both experiments were conducted

at 20 ℃. The test tubes were mixed at 30 rpm for 60 min, after which the solution was separated from the PBP-IOPs using a magnetic bar and analyzed for P_i.

To evaluate the performance of PBP-IOPs in more realistic scenarios, another batch experiment was performed using tertiary wastewater effluent compared to an equal concentration of P_i-only solution. Tertiary wastewater effluent was collected from the South Shore Water Reclamation Facility (Oak Creek, WI), and analyzed for water quality parameters (Table S1). The initial P_i concentration was 1.2 mg PO_4^{3-} L^{-1}. Other experimental conditions (adsorbent dosage, time, and mixing speed) were identical to the multi-ion solution test.

2.5 Reusability of PBP-IOPs

Recovering P_i as a concentrated solution is important for subsequent reuse. The PBP-IOPs must also be reusable such that the P_i binding ability of the system is restored following desorption (28). To test desorption, an adsorption experiment was first conducted with an initial P_i concentration of 0.9 mg PO_4^{3-} L^{-1} and 20 mg PBP-IOPs for 30 min in 1 mL reaction buffer (pH 7, 20 ℃). The desorption experiment was performed using 1 mL of Tris buffer at pH 11.5 for 10 min, which was previously reported to completely desorb P_i from PBP (18). In parallel, unmodified IOPs (20 mg NHS-activated IOPs without PBP immobilized on the surface) were tested for P_i adsorption and desorption under identical experimental conditions to the PBP-IOP tests.

2.6 Determination of Phosphate Removal Capacity

2.6.1 Phosphate Adsorption Isotherms

Phosphate adsorption isotherms were investigated by varying the initial concentration of P_i while maintaining a constant dose of PBP-IOPs. The P_i solution was prepared in Tris buffer at pH 7, 20 ℃ at concentrations of 0.2, 0.4, 0.6, 0.8, or 1 mg PO_4^{3-} L^{-1}. Low initial concentrations were selected to reflect tertiary wastewater treatment needed to reduce low P_i levels to ultra-low

discharge standards. A dose of 20 mg PBP-IOPs was allowed to react with 1 mL P_i solution for 60 min. The samples were mixed at 30 rpm using a multi-purpose tube rotator at room temperature. Once the test was completed, the reaction solution was separated from the PBP-IOP adsorbent using a magnetic bar and was analyzed for remaining P_i. The data was then modeled using Langmuir and Freundlich isotherm models (Equations 4 and 5, respectively).

$$q_e = \frac{q_{max} K_L C_e}{(1 + K^L C^e)} \qquad \text{(Eq 4)}$$

$$q_e = K_F C_e^{1/n} \qquad \text{(Eq 5)}$$

where q_e is the equilibrium adsorption capacity (mg g^{-1}), q_{max} is the maximum adsorption capacity (mg g^{-1}), C_e is the equilibrium P_i concentration (mg L^{-1}), K_L is the Langmuir constant (L mg^{-1}), K_F is the Freundlich constant (mg g^{-1}), and n defines the intensity of the adsorption process (dimensionless constant). The Langmuir model parameter K_L indicates the adsorption affinity between the adsorbate and the adsorbent and is related to energy of adsorption (ΔG) and enthalpy change (ΔH).

2.6.2 Theoretical P_i Adsorption Capacity

Calculations were performed to estimate the theoretical maximum P_i binding capacity of PBP-IOPs and PBP immobilized on NHS activated Sepharose resin in comparison to experimental results. The theoretical P_i adsorption capacity was determined under scenarios of 1) maximum available NHS ligand usage (the number of sites available to covalently link a protein, referred to as "ligand-based capacity" in this study) and 2) space occupied by the PBP protein on the available surface area (referred to as "footprint-based capacity" in this study). Further description of these theoretical calculations is included in the Supporting Information (SI).

2.7 Molecular Dynamics Simulations of P_i Binding to PBP

The interaction of P_i (modeled as dihydrogen phosphate, $H_2PO_4^-$) with PBP was investigated using all-atom MD simulations with the AMBER 2019 software package (29). Two types of simulations were conducted: one involving PBP with a single $H_2PO_4^-$ ion initially in the bound position, and the other with a higher P_i concentration, where PBP had 10 initially unbound $H_2PO_4^-$ ions placed randomly around PBP. The initial structure of the PBP was obtained from the Protein Data Bank (PDB ID 1A54) (30). The GAFF2 force field was used for $H_2PO_4^-$, and the partial charges were calculated using geometric optimization and the restrained electrostatic potential (RESP) charge fitting, performed by R.E.D. Server Development (31). The ff19SB force field (32) was used for PBP with TIP3P water model (33) with corresponding Joung-Cheatham monovalent ion parameters (34). The PBP was solvated in a water box with an 8 Å buffer and Na^+ ions to neutralize the total charge of the system. The pre-production of the MD simulations followed the 12-step protocol previously described in detail (35,36) and included seven energy minimization stages with up to 115,000 total steps, 2 heating, and 3 equilibration stages. The final NPT production simulations were performed at 1 bar and 300 K with a cutoff of 9.0 Å and a timestep of 2 fs for a period of 1 and 2 μs for the single- and multiple-ion simulations, respectively. Analysis was performed using CPPTRAJ (37). Total contact lifetime between the $H_2PO_4^-$ ions and the PBP was calculated using PyContact (38).

2.8 Experimental Data Analysis

All experiments were performed in triplicate. One-way ANOVA followed by Tukey post-hoc analysis was performed to assess differences in P_i removal efficiency under different experimental conditions (pH, temperature, and ionic strength) as well as for selectivity and reusability studies. All statistics were performed using GraphPad Prism with a significance level of $\alpha = 0.05$.

3 Results and Discussion

3.1 Phosphorus Adsorption Kinetics

Pseudo first- and second-order kinetic models were applied to quantify the rate of adsorption, an important parameter for scaled treatment systems. The pseudo first-order model assumes the rate-limiting step depends on collisions between the adsorbate and the unoccupied sites at the surface of adsorbent, whereas the pseudo second-order model assumes diffusion as the rate limiting step (39). We observed that the pseudo second-order kinetic model provided a slightly better fit over the pseudo first-order model (Figure 1), suggesting diffusion-limited adsorption of P_i using PBP-IOPs. Most of the adsorbed P_i was rapidly removed within 5 min and the system reached equilibrium after 10 min as there was no change in the adsorbed P_i for longer times. The strong pseudo second-order kinetic model fit supports findings by Venkiteshwaran et al. (2020) (17), in which PBP was immobilized on NHS-activated Sepharose beads.

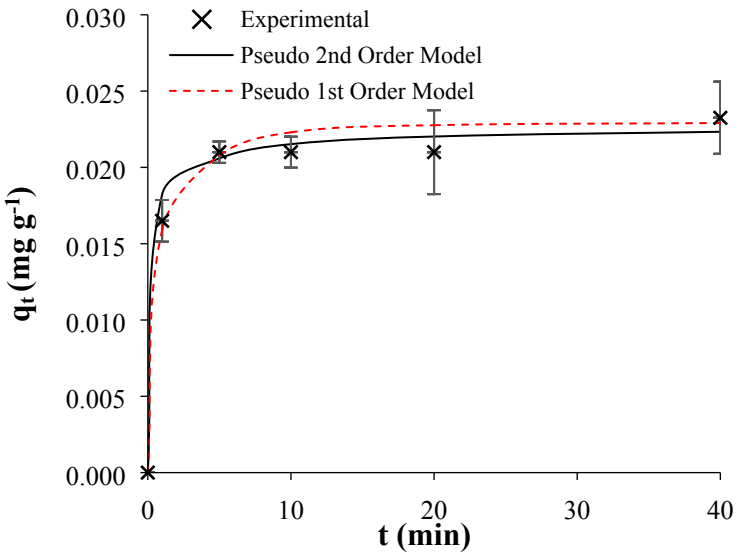

Figure 1. Experimental data fit to the nonlinear form of the pseudo first- and second-order kinetic models using PBP-IOPs at neutral pH and 20 ℃. The pseudo first-order model parameters were k_1

= 2.35 min^{-1} and q_e = 0.023 mg g^{-1}, (R^2 =0.98). The pseudo second-order model parameters were k_2 = 283 g $mg^{-1}min^{-1}$ and q_e = 0.024 mg g^{-1} (R^2 =0.99). The linear model fits are shown in Figures S1 and S2.

Using PBP-IOPs, the kinetic rate constant (k_2) was substantially higher than most other comparative adsorbents used to remove P_i (Table 1). The kinetic model also indicated that the equilibrium capacity (q_e, mg g^{-1}) for PBP-IOPs was approximately 3.6 times greater than that for PBP immobilized on Sepharose. However, the equilibrium capacity, q_e, for PBP-IOPs was still less than other non-PBP adsorbents; the maximum capacity is discussed in Section 3.5.

To further explore differences between the PBP adsorbents prepared using different immobilization materials (Sepharose vs. IOPs), the pseudo second-order kinetic model parameters were normalized to PBP binding sites (i.e., per mole PBP) to establish performance relative to the functional unit rather than the mass of the adsorbents (Table 1). Using this approach, the equilibrium capacities of the two PBP-based adsorbents were similar (q_e = 0.64 vs. 0.86 mol P_i mol^{-1} PBP). However, the rate constant for PBP-Sepharose was approximately 3.5 times higher than the rate constant for PBP-IOPs. This variation could be attributed to the difference in the ligand density between the materials, which may affect PBP orientation/attachment on the surface (40), consequently affecting the rate of access to the PBP binding sites. Of note, the initial sorption rate when time goes to 0 ($k_2*q_e^2$) (41) of the two PBP adsorbents was very similar, at 0.21 mg g^{-1} min^{-1} for PBP-Sepharose and 0.17 mg g^{-1} min^{-1} for PBP-IOPs, which suggests similar binding rates for PBPs not influenced by steric hindrance on IOPs and Sepharose resin.

Table 1. Pseudo second-order kinetic parameters for several comparative P-selective adsorbents.

Adsorbent	Pseudo Second-order Kinetic Parameters		Study
	k_2 (g $mg^{-1}min^{-1}$)	q_e (mg g^{-1})	
Zeolite (EL-MNP@zeolite)	0.013	38.6	(42)
Ferrihydrite	$4x10^{-4}$	40.3	(43)
Ferrihydrite-impregnated granular activated carbon (FH@GAC)	1.85	1.26	(6)
Iron hydroxides (FeOOHs)	0.25	4.5	(44)
Granular ferric hydroxide	0.04	0.64	(45)
Zinc oxide nanoparticles (ZnO)	0.01	54.6	(46)
PBP immobilized on Sepharose resin	$4.9x10^3$ (37.5 mol PBP mol^{-1} P_i min^{-1})*	0.0066 (0.86 mol P_i mol^{-1} PBP)*	(17)
PBP-IOPs	283 (10.6 mol PBP mol^{-1} P_i min^{-1})*	0.024 (0.64 mol P_i mol^{-1} PBP)*	This study

* Normalized values of k_2 and q_e on a mole PBP basis, calculated using the nonlinear pseudo second-order model parameters.

3.2 Effect of pH, Temperature, and Ionic Strength

Increasing pH from 4 to 10 significantly decreased P_i removal from 50% to less than 10% (Figure 2a, $p < 0.0001$). However, P_i removal at acidic conditions (pH 4 and 6) did not differ significantly ($p = 0.64$). Solution pH affects both the degree of adsorbate dissociation and adsorbent surface charge (47). Phosphate deprotonates as pH increases, progressing from $H^3PO^4 \rightarrow H_2PO_4^- \rightarrow HPO_4^{2-} \rightarrow PO_4^{3-}$, corresponding to the acid dissociation constants pKa_1=2.15, pKa_2=7.2, and pKa_3=12.33 (48). Accordingly, pH controls the distribution of dominant P_i species and influences the strength of electrostatic attraction. While PBP has a strong affinity for $H_2PO_4^-$

and HPO_4^{2-}, with a slight preference for the latter (49), strong competition occurs between P_i species and hydroxyl functional groups, consequently creating strong repulsion and reducing adsorption as the pH increases (48).

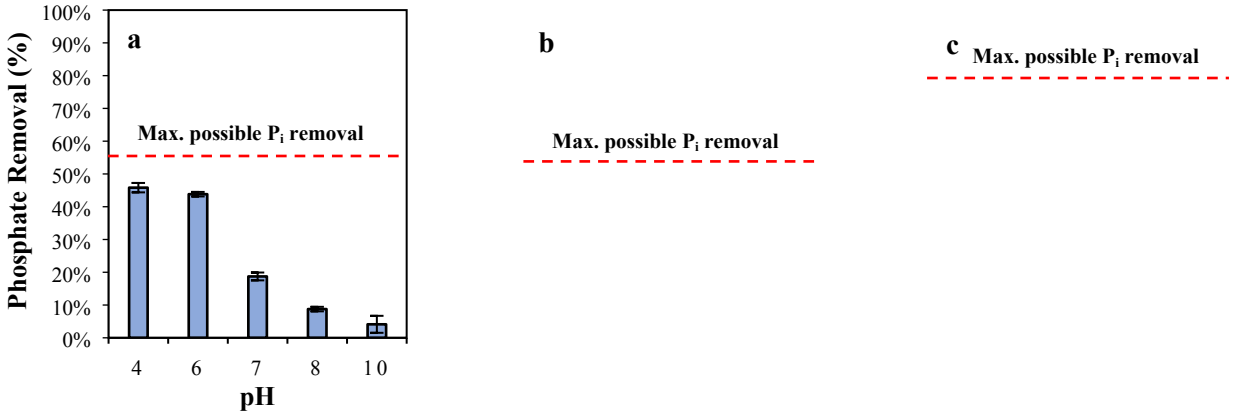

Figure 2. Effect of (a) pH (with constant temperature = 20 ℃ and ionic strength = 0 M KCl), (b) temperature (with constant pH = 7 and ionic strength = 0 M KCl), and (c) ionic strength (KCl addition) (with constant pH = 7 and temperature = 20 ℃) on phosphate adsorption using PBP-IOPs. Triplicate experiments were conducted for 60 minutes, and results are shown as averages with ± 1 standard deviation denoted by the error bars. The dashed-red lines indicate the maximium possible P_i removal based on the amount of immobilized PBP used in the test relative to the initial P_i concentration in the solution.

Beyond affecting P_i protonation/deprotonation, the surface charge of an adsorbent may affect P_i adsorption as more positive charges accumulate below the point of zero charge (pH_{pzc}) and more negative charges exist above the pH_{pzc}. For PBP-IOPs, the surface charge of the base material (i.e., iron oxide) is not subject to changes in speciation as a function of pH due to the presence of a silicon coating (50). Therefore, pH would more likely affect PBP's binding sites and trigger conformational changes. A fluorescent thermal shift assay showed that changes in pH did not significantly alter the thermal stability of PBP (18). Hence, high pH is unlikely to significantly alter PBP structure; however, changes in the coordination structure of the local binding site could affect P_i adsorption. PBP binds P_i via amino acids with pK_a values ranging from 9.04 to 9.6 (49),

so deprotonation is most likely to occur at pH > 10, thereby inhibiting hydrogen bond formation between P_i and the PBP binding site.

Removal of P_i as a function of temperature (a crucial factor for adsorption at liquid-solid interfaces) is presented in Figure 2b. The highest removal was at 20 ℃ and the lowest at 10 ℃ ($p = 0.003$). Adsorption behavior was similar at 10, 30, and 40 ℃ ($p \leq 0.18$), all of which were worse for P_i removal compared to 20 ℃. Venkiteshwaran et al. (2020) (17) calculated the thermodynamic parameters for P_i adsorption using PBP immobilized on Sepharose resin and confirmed a spontaneous, exothermic process: the estimated enthalpy change (ΔH) was approximately -6.3 kJ mol^{-1}, the calculated entropy change (ΔS) was 0.12 kJ mol^{-1} K^{-1}, and Gibbs free energy (ΔG) was negative (17). Consistent with the proposed P_i-PBP interaction at the binding site (i.e., formation of 12 hydrogen bonds), noncovalent interactions such as van der Waals forces, hydrogen bonds, and ionic pairs are indicated by low enthalpy changes (ΔH < 80 kJ mol^{-1}) (51). Alternately, P_i removal is endothermic (requiring an energy input to drive adsorption) using many other adsorbents such as ferrihydrite, magnetite, or lanthanum-doped activated carbon fiber, as indicated by an increase in P_i uptake with increasing temperature (48,52). Therefore, P_i removal using PBP adsorbents is advantageous over other adsorbents as no energy addition is needed, promoting efficient P_i removal.

Removal of P_i significantly decreased from 66% to 6% when the concentration of KCl (ionic strength) increased 50-fold from 0.01 to 0.5 M (Figure 2c, $p < 0.0001$). Although there is no competition on the binding site due to the high selectivity of PBP toward P_i, poorer P_i removal was observed using PBP-IOPs at high ionic strength (> 0.01 M KCl), indicating interrupted PBP binding affinity (53,54). The dissociation constant for the PBP-P_i complex (K_d) increased approximately 20 times for 0.3 M of NaCl solution compared to no-salt solution (53). The affinity

of PBP for P_i was found to be extremely sensitive to electrostatic effects at the level of local hydrogen bonding interactions (53). Therefore, increasing ionic strength impeded the formation of hydrogen bonds in the binding site and decreased P_i uptake.

3.3 Selectivity of PBP-IOPs

To evaluate the P_i removal performance of PBP-IOPs in more practical conditions, PBP-IOPs were tested in multi-ion solution as well as tertiary wastewater effluent (Figure 3). The adsorption capacity of the PBP-IOPs for both tests was 40 μg-P_i g^{-1}. Removal of P_i was identical for P_i-only solution and multi-ion solution (22%, $p = 0.99$). Similarly, P_i removal for tertiary wastewater effluent was the same as the corresponding P_i-only solution (17%). Thus, the selectivity of the PBP-IOPs was not affected by the presence of competing anions such as chloride, sulfate, nitrate, bicarbonate, and borate.

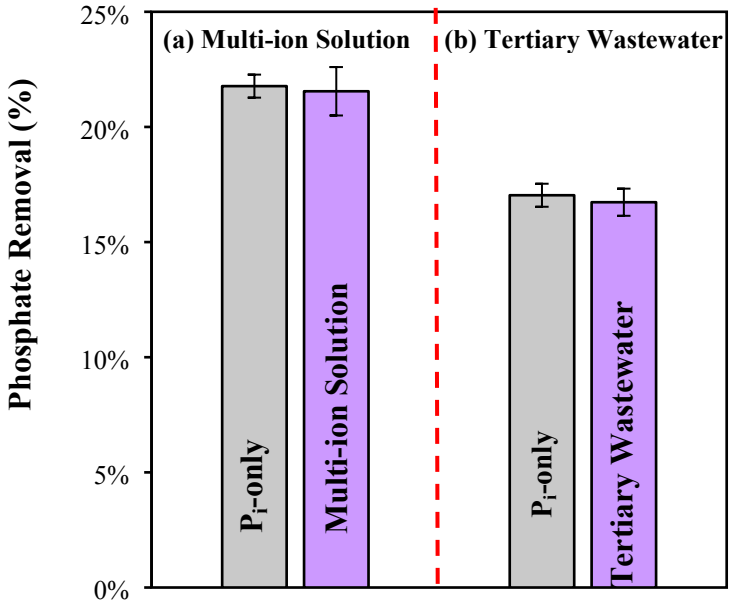

Figure 3. Phosphate adsorption using PBP-IOPs is not impacted by other water constituents. (a) multi-ion solution with 1 mg L^{-1} each of NaCl, Na_2SO_4, $NaNO_3$, $NaHCO_3$, $B_4Na_2O_7 \cdot 10H_2O$, and KH_2PO_4 versus P_i-only solution containing 0.9 mg L^{-1} KH_2PO_4 (0.63 mg P_i L^{-1}). (b) tertiary wastewater versus P_i-only solution, each containing 1.2 mg L^{-1} KH_2PO_4 (0.85 mg P_i L^{-1}). All experiments were conducted in triplicate, with ± 1 standard deviation indicated by the error bars.

The results agree with a previous selectivity study of PBP immobilized on Sepharose resin, in which competitive anions did not impede P_i removal (14). In comparison, water constituents (i.e., anions, total suspended solid, and dissolved organic carbon) substantially reduced P_i removal efficiency using commercial ferric nanoparticles and hybrid anion resin (HAIX) (7). HAIX resin lost up to 36% of its P_i adsorption capacity when preloaded with nitrate in synthetic water trials (7). Trials using secondary wastewater had greater impact on HAIX removal capacity since both nitrate preloading and simultaneous competition from the other constituents in secondary wastewater were involved (7). Using synthetic solution, ferric nanoparticles had 76% less P_i capacity compared to HAIX resin (7). PBP-IOPs provide highly selective P_i removal with no impedance from competing ions, offering an advantage over other adsorbents such as HAIX or ferric nanoparticles.

3.4 Reusability of PBP-IOPs

To assess the reusability of PBP-IOPs in comparison to iron oxide adsorbents, the P_i adsorption-desorption capacities of unmodified IOPs (i.e., bare IOPs without NHS activation or PBP attached) and PBP-IOPs were compared in head-to-head tests (Figure 4). PBP-IOPs were able to remove 0.30 mg PO_4^{3-} L^{-1} while IOPs alone removed 0.67 mg PO_4^{3-} L^{-1} under the same experimental conditions, indicating more active adsorption sites on IOPs compared to PBP-IOPs, perhaps due to space limitations of PBP loading on the IOP surface (as explored in Section 3.5.2). However, PBP-IOPs released 0.30 mg PO_4^{3-} L^{-1} (99% of total adsorbed P_i) whereas IOPs released only 0.08 mg PO_4^{3-} L^{-1} (12% of total adsorbed P_i) after exposure to Tris buffer at pH 11.5. This important finding demonstrated that PBP-IOPs may offer an improved approach to recover P_i (compared to IOPs alone) wherein nearly all adsorbed P_i can be recovered.

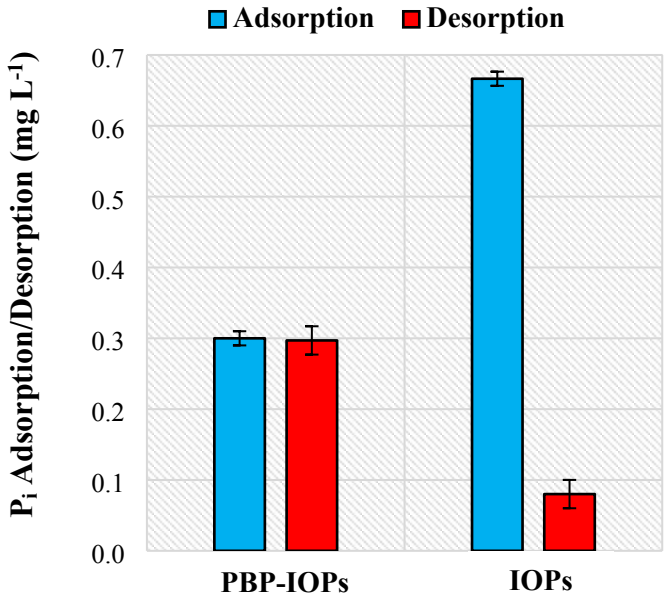

Figure 4. Comparsion of changes in phosphate concentration for adsorption and desorption stages using IOPs modified with PBP and unmodified IOPs. All experiments were conducted in triplicate, with ± 1 standard deviation indicated by the error bars.

3.5 Adsorption Capacity

3.5.1 Phosphorus Adsorption Isotherms

Langmuir and Freundlich isotherms were used to model the profile of the equilibrium adsorption capacity (q_e) and the equilibrium P_i concentration (C_e) (Figure 5). The experimental data fit both models well, with $R^2 \geq 0.99$. Although the models had identical profiles up to 0.6 mg L^{-1}, they diverged at higher C_e values, where the Langmuir model provided a better nonlinear fit ($K_L = 1.0$ L mg^{-1}, $q_{max} = 0.036$ mg g^{-1}). The Langmuir model assumes monolayer adsorption, where each active site is occupied by one adsorbate molecule, in line with the expected 1:1 PBP-P_i binding scenario.

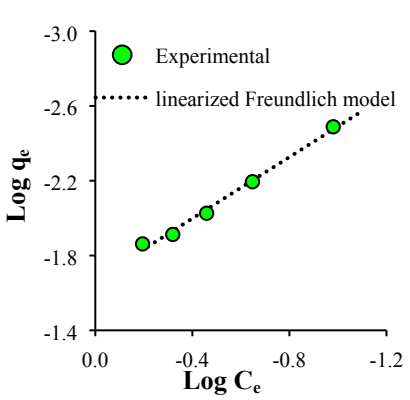

Figure 5. Phosphate adsorption isotherms using PBP-IOPs at neutral pH and 20 ℃. (a) Experimental data fit to nonlinear isotherm models, where the error bars indicate ±1 standard deviation of triplicate experiments, (b) linearized Langmuir model (K_L = 0.753 L mg^{-1}, q_{max} = 0.044 mg g^{-1}), and (c) linearized Freundlich model (K_F = 0.021 mg g^{-1}, n =1.218).

The Langmuir constant (K_L) can be used to determine the feasibility of P_i adsorption by calculating the dimensionless separation factor (R_L, Equation 6) (55):

$$R_L = \frac{1}{1 + K^L C^0} \qquad \text{Eq (6)}$$

where R_L = 0 indicates irreversible adsorption, 0 < R_L <1 indicates favorable adsorption, R_L = 1 indicates a linear ($q_e$vs. C_e) adsorption curve, and R_L > 1 indicates unfavorable adsorption (46,48). For this dataset, R_L was 0.6-0.9, indicating favorable adsorption. The Freundlich constant (n) fell in the range of 0-10, also indicating favorable adsorption (56).

The adsorption affinity (K_L) for PBP-IOPs was 7 to 24 times higher compared to other adsorbents such as ZnFeZr-coated magnetic particles, flower-like mesoporous silica loaded with lanthanum, humic acid-coated magnetite nanoparticles, and iron oxide-coated granular activated carbon (Table 2). However, the K_L for PBP-IOPs was approximately two orders of magnitude less than PBP-Sepharose.

Using both PBP-based adsorbents, the maximum adsorption capacity (q_{max}) was less than the comparative adsorbents (Table 2). However, PBP-IOPs provided approximately six times

higher maximum capacity than the P_i adsorption capacity using PBP immobilized on Sepharose resin (17). The enhanced capacity likely derived from having more PBP immobilized on IOPs relative to Sepharose resin (which leads to higher P_i removal). The average particle size of the IOPs was 1 μm with an NHS ligand density of 250 μmol per g IOPs, while NHS-activated Sepharose was 90 μm with an NHS ligand density of 33 μmol per g Sepharose beads. Therefore, higher ligand density was available to conjugate PBP on IOPs compared to NHS-activated Sepharose.

When normalizing the Langmuir parameters to PBP binding sites (i.e., per mole PBP), the maximum capacities for PBP-IOPs and PBP-Sepharose were essentially equivalent (q_{max} 0.96 and 0.90 mol P_i mol^{-1} PBP, respectively). However, the P_i binding affinity (K_L) using PBP-IOPs remained two orders of magnitude less than PBP-Sepharose, indicating that the less dense NHS configuration had stronger interactions. Thus, while the higher ligand density of IOPs improved the maximum P_i adsorption capacity, it may have affected conformation of PBP on the surface, which negatively impacted binding affinity (40).

Table 2. Langmuir isotherm parameters for P-selective adsorbents.

Adsorbent	Langmuir Isotherm Parameters		Study
	K_L (L mg^{-1})	q_{max} (mg g^{-1})	
Flower-like mesoporous silica spheres doped with lanthanum (FMS-0.1 La)	0.11	6.1	(57)
Tailored ZnFeZr-coated magnetic particles (ZnFeZr @ Fe_3O_4/SiO_2)	0.1	32.2	(58)
Humic acid-coated magnetite nanoparticles (HA-MNP)	0.03	3.0	(59)
Iron oxide-coated granular activated carbon (Fe-GAC)	0.08	21.8	(60)
PBP immobilized on Sepharose resin	192 (18.2 μM^{-1} P_i)*	0.0062 (0.90 mole P_i $mole^{-1}$ PBP)*	(17)
PBP-IOPs	1.0 (0.095 μM^{-1} P_i)*	0.036 (0.96 mole P_i $mole^{-1}$ PBP)*	This study

* Normalized values of K_L and q_{max} on a mole PBP basis, calculated using the nonlinear Langmuir isotherm model parameters.

3.5.2 Theoretical Scenarios for Adsorption Capacity

A series of theoretical calculations was performed to further explore the P_i adsorption capacity for PBP-IOPs compared to PBP immobilized on Sepharose resin (methods described in SI Section S3). First, the impact of surface area to mass ratio on adsorption capacity was calculated (Figure 6a, where the 1-µm diameter IOPs offered 10x more surface area [1.1 m^2 g^{-1}] than an equivalent mass of Sepharose [$9.5x10^{-2}$ m^2 g^{-1}]). The calculation was performed based on the reported NHS ligand density on IOPs (250 µmol NHS per g IOPs) vs. Sepharose resin (33 µmol

NHS per g Sepharose beads) as well as based on the physical footprint of PBP (cross-sectional area of PBP per surface area of adsorbent). As shown, the major limitation for improvements in P_i adsorption capacity is the size of the protein itself, which prevents full usage of the available ligands. Comparing PBP adsorbent performance to other adsorbents in the literature (as detailed in the SI), if all NHS ligand sites were occupied by PBP, both IOPs and Sepharose resin-based adsorbents would be competitive with approximately half of the comparative adsorbents. However, the surface area to mass ratio would more realistically need to increase nearly 100x to begin to compete with other adsorbents. This indicates that simply decreasing the particle size of the base material is insufficient to make PBP-based adsorbents more competitive in terms of P_i adsorption capacity. Accordingly, strategies for improved capacity may emphasize immobilization on porous materials with higher surface to mass ratios and/or decreased size of the PBP to a shorter P_i-selective peptide sequence.

a

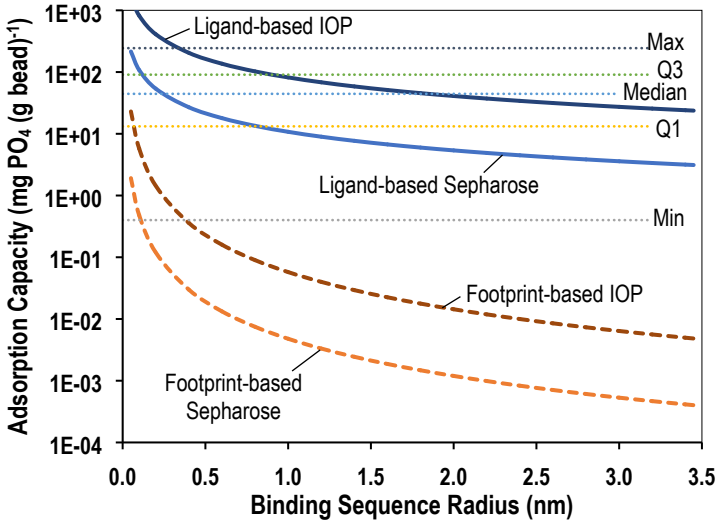
Adsorption Capacity (mg PO4 (g bead)-1)
1E+03
1E+02
1E+01
1E+00
1E-01
1E-02
1E-03
1E-04
Ligand-based IOP
Max
Q3
Median
Q1
Ligand-based Sepharose
Min
Footprint-based IOP
Footprint-based Sepharose
0.0
0.5
1.0
1.5
2.0
2.5
3.0
3.5
Binding Sequence Radius (nm)

b

c

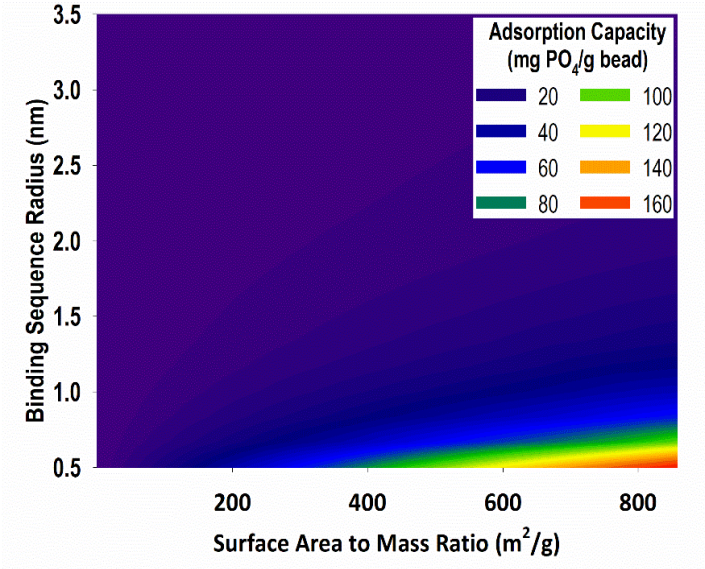
Binding Sequence Radius (nm)
3.5
3.0
2.5
2.0
1.5
1.0
0.5
Adsorption Capacity (mg PO4/g bead)
20
40
60
80
100
120
140
160
200
400
600
800
Surface Area to Mass Ratio (m2/g)

Figure 6. Theoretical adsorption capacity scenarios. (a) Adsorption capacity as a function of surface area to mass ratio, (b) Adsorption capacity as a function of peptide sequence radius, and (c) Adsorption capacity as a function of both surface area to mass ratio and peptide sequence radius. For illustrative purposes, the 40 different comparative values for adsorbents reported in the literature shown in (a) and (b) are summarized by quartiles (Q1 = first quartile and Q3 = third quartile) and min, median, and max values. Table S2 lists all comparative values.

The impact of reducing the peptide sequence size is shown in Figure 6b, where PBP itself is approximately 3.45 nm in radius (with a theoretical lower limit of 0.2 nm based on our analysis of the size of PBP's active binding pocket). Future research is needed to demonstrate whether peptides with reduced sequences retain P_i attachment efficiency and selectivity. The limiting factor is again clearly shown to be the size of the binding sequence as opposed to the availability of NHS ligands. If all ligands were occupied with PBP on either IOPs or Sepharose resin materials, the PBP-based adsorbent would be strongly competitive with other materials (using PBP, the capacity would be approximately average that of other reported materials, whereas a 10-fold decrease in polypeptide size would exceed the capacity for all comparative adsorbents included here). However, accounting for the size of the binding sequence, nearly 10-fold decrease in the size of the P_i-selective polypeptide sequence would be needed to compete with the lowest adsorption capacity of the competitive benchmarks included here. Accordingly, parallel improvements in binding sequence size (while retaining P_i selectivity) and surface area to mass ratio of the base material are recommended to further advance design and implementation of PBP-based adsorbents (Figure 6c). The prospect of reducing the binding sequence size is discussed further in the following section.

3.6 PBP-P_i Binding Modeled using All-atom Molecular Dynamics

To understand how P_i interacts with PBP and to assess the feasibility of reducing the size of the P-binding sequence for increased capacity of PBP-based adsorbents, we performed all-atom

MD simulations at various P_i concentrations. First, we examined the structure of PBP with P_i bound in the position as observed in the crystal structure (Figure 7a), where P_i specifically interacts with the ALA 9, THR 10, PHE 11, GLY 37, SER 38, ASP 56, ARG 135, SER 139, GLY 140, and THR 141 amino acids (61). We calculated the temporal profile (Figure 7b) of the distance between the centers of mass (COM) of section one, which includes residues 1-76 and 227-321 (COM1 in Figure 7a), and section two, which includes residues 77 to 226 (COM2 in Figure 7a). The two sections were visually determined to separate two large portions of PBP that appeared to be gyrating with respect to one another. We found that the P_i binding/release event requires a hinge-like motion by the protein. While $H_2PO_4^-$ was in the bound position (Figure 7a), the distance between COM1 and COM2 was approximately 27.7 Å. However, $H_2PO_4^-$ leaves the binding pocket after approximately 130 ns, at which time the distance between the COMs increases to about 29.7 Å (Figure 7b). In addition to the increase in the distance between COMs, there is also a clear increase in overall motion of the two sections relative to each other upon unbinding.

To test the specificity of P_i-PBP binding, MD simulations with 10 unbound $H_2PO_4^-$ were performed. While none of the ten $H_2PO_4^-$ ions fully bound to the pocket of PBP, possibly due to insufficient simulation time, the interactions between the $H_2PO_4^-$ ions and PBP were frequent and highly specific to the binding pocket. Atom-atom contacts between $H_2PO_4^-$ and PBP were then analyzed using a contact distance criterion of 5.0 Å, which is the default for PyContact for protein structure networks (62,63). Atom-atom contacts were accumulated over residues to obtain P_i-amino acid contact data. Amino acids with a total contact lifetime of more than 250 ns are plotted in Figure 7c, where the thickness of the lune represents the value of the lifetime. These amino acids are all located within the same region of PBP (Figure 7d) and contained all of the amino acids located within the known binding site (ALA 9, THR 10, PHE 11, GLY 37, SER 38, ASP 56, ARG

135, SER 139, GLY 140, and THR 141) (30) and proximal additional amino acids (GLY138, GLU195, ASP 137, SER39, and ASN177). Overall, our simulations determined that P_i binding requires a hinge motion in the binding site and 15 critical amino acids. Thus, reductions in the protein's size are non-trivial due to the hinge motion.

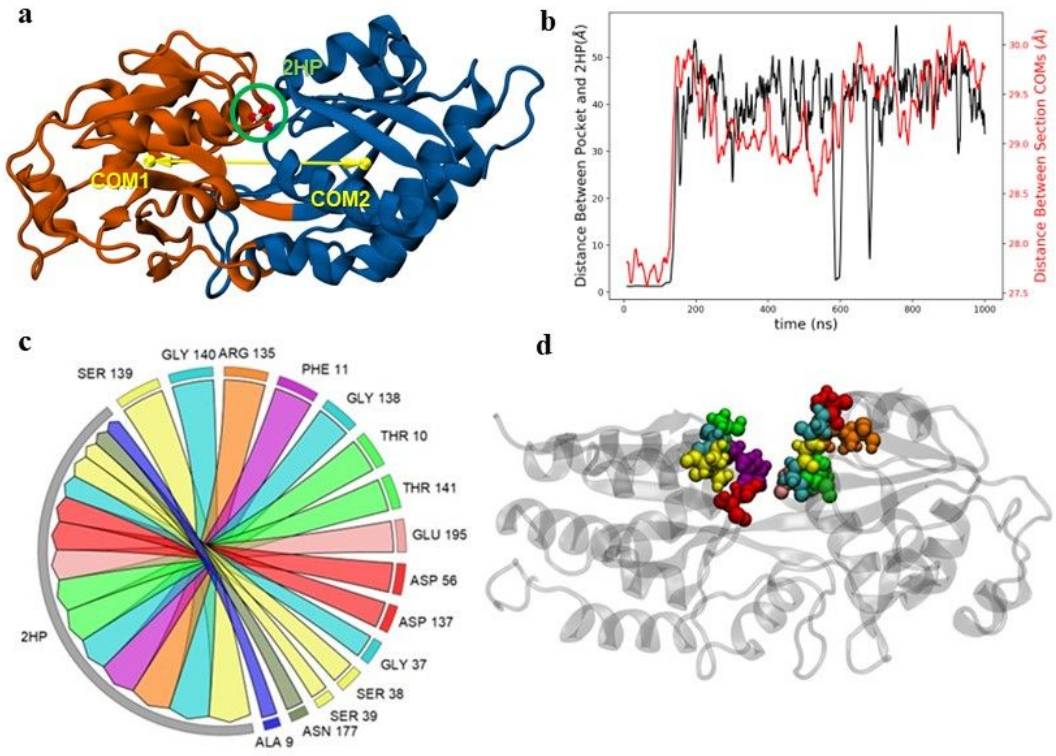

Figure 7. (a) Initial structure of PBP with a single $H_2PO_4^-$ ion bound (green circle, "2HP" notation). The yellow arrow shows the distance between two sides defined as center of mass (COM) for residues 1-76 and 227-321 (COM1) and section two for residues 77 to 226 (COM2). (b) Temporal profiles of the distance between COM1 and COM2 (red) and the distance between the PBP binding pocket and $H_2PO_4^-$ (black) for a single $H_2PO_4^-$ in the simulation. (c) Chord diagram representing total contact lifetime of each amino acid with $H_2PO_4^-$ for the multiple $H_2PO_4^-$ simulation. Only amino acids with total contact lifetimes greater than 250 ns are shown. (d) PBP structure with the amino acids from the chord diagram colored accordingly and displayed in ball-and-stick representation.

The importance of the hinge motion potentially complicates efforts to design a shorter peptide sequence that retains its ability to effectively bind P_i. Removing any of the amino acids

that are crucial to enabling hinge motion or locking it out upon binding would jeopardize the PBP's binding propensity. Our results showed that amino acids critical to this motion span a substantial length of the peptide (residues 9 to 177), and this span may represent an inherent lower limit to the extent of shortening the peptide sequence before losing its P_i specificity. While the hinge motion is thus important, several studies provide substantial evidence supporting the feasibility of designing and synthesizing peptide sequences that leverage functional amino acid sequences derived from proteins (64–66). For example, Fowler et al. (2021) (67) demonstrated selective P_i adsorption and controlled desorption using a protein-derived P_i-binding peptide sequence approximately 37x smaller than the PBP tested in our study. Immobilization of such peptide sequences and testing their P_i binding potential in a range of conditions relative to water/wastewater is important moving forward to further evaluate the adsorbent's abilities relative to other adsorbents.

4 Conclusions

A PBP-loaded IOP adsorbent was hypothesized to improve P_i adsorption capacity over previous PBP systems and to provide enhanced P_i recovery potential compared to unmodified IOPs. Using PBP-IOPs, P_i adsorption kinetics demonstrated rapid P_i removal, providing more than 95% adsorption within 5 min. Slightly acidic pH (6), 20 ℃ temperature, and low ionic strength (0.01 M KCl) conditions demonstrated the best removal efficiency. The removal capacity of PBP-IOPs was not affected by competing anions such as chloride, sulfate, nitrate, bicarbonate, and borate. PBP-IOPs released 99% of total adsorbed P_i under controlled conditions. These results underscore the ability of the PBP-IOP adsorbent to adsorb P_i rapidly, selectively, and reversibly. Importantly, PBP-based adsorbents feature much higher P_i binding affinity (approximately ≥10

times more) compared to other adsorbents in literature (Table 2). Moreover, PBP-IOPs offered superior ability to recover P_i compared to unmodified IOPs, which is essential to promote not only P_i removal, but also recovery as part of a circular phosphorus economy. Future studies assessing long-term stability of the PBP-IOP adsorbent would further advance understanding of its use in full-scale wastewater treatment applications.

Monolayer adsorption (Langmuir model) characterized PBP-IOP interactions with P_i. Conjugation of PBP to higher surface area IOPs (i.e., smaller particle size) increased the overall P_i attachment capacity relative to PBP immobilized on NHS-activated Sepharose beads. The PBP-IOP adsorbent enhanced the removal capacity of P_i compared to previous PBP systems (i.e., PBP immobilized on Sepharose resin). Yet, P_i removal capacity was still low compared to other adsorbents. Future work to improve P_i capacity should include improvements in the base immobilization material as well as working with smaller biomolecules such as pared down peptide sequences retaining the selective P-binding capabilities provided by the amino acid residues present in the binding pocket of PBP. Designing engineered peptides to capture and release P_i would not only simulate the functionality of natural proteins but also boost P_i removal capacity by increasing the attachment density of the functionalized material.

Declaration of Competing Interests

B.K. Mayer is a co-inventor on a patent application entitled “Process for controlled adsorption and desorption of phosphate from liquids using phosphate-selective proteins”. The authors declare no other potential conflicts of interest.

Acknowledgements

This project was supported by the Science and Technologies for Phosphorus Sustainability (STEPS) Center under National Science Foundation (NSF) award number CBET-2019435. All conclusions are those of the authors and do not necessarily reflect the views of the NSF. We thank Paige Peters and Ashley Tan from the Water Quality Center at Marquette University for their help in collecting samples of the tertiary wastewater effluent and measuring phosphate concentrations. We also thank Dr. Venkiteshwaran from the University of South Alabama for his thoughtful discussions related to the kinetic and isotherm calculations for PBP immobilized on Sepharose resin.

References

1. Dodds WK, Smith VH. Nitrogen, phosphorus, and eutrophication in streams. Inland Waters. 2016;6(2):155–64. Available from: https://doi.org/10.5268/IW-6.2.909
2. Bui TH, Hong SP, Yoon J. Development of nanoscale zirconium molybdate embedded anion exchange resin for selective removal of phosphate. Water Res. 2018 May 1;134:22–31. Available from: https://doi.org/10.1016/j.watres.2018.01.061
3. Huang H, Zhang DD, Li J, Guo G, Tang S. Phosphate recovery from swine wastewater using plant ash in chemical crystallization. J Clean Prod. 2017 Dec 1;168:338–45. Available from: https://doi.org/10.1016/j.jclepro.2017.09.042
4. Mayer BK, Gerrity D, Rittmann BE, Reisinger D, Brandt-Williams S. Innovative strategies to achieve low total phosphorus concentrations in high water flows. Crit Rev Environ Sci Technol. 2013;43:409–41. Available from: https://doi.org/10.1080/10643389.2011.604262
5. Oehmen A, Lemos PC, Carvalho G, Yuan Z, Keller J, Blackall LL, et al. Advances in enhanced biological phosphorus removal: From micro to macro scale. Vol. 41, Water Research. 2007:2271–300. Available from: https://doi.org/10.1016/j.watres.2007.02.030
6. Mahardika D, Park HS, Choo KH. Ferrihydrite-impregnated granular activated carbon (FH@GAC) for efficient phosphorus removal from wastewater secondary effluent. Chemosphere. 2018;207:527–33. Available from: https://doi.org/10.1016/j.chemosphere.2018.05.124
7. Muhammad A, Soares A, Jefferson B. The impact of background wastewater constituents on the selectivity and capacity of a hybrid ion exchange resin for phosphorus removal

from wastewater. Chemosphere. 2019;224:494–501. Available from: https://doi.org/10.1016/j.chemosphere.2019.01.085

8. Qiu H, Liang C, Yu J, Zhang Q. Preferable phosphate sequestration by nano-La(III) (hydr)oxides modified wheat straw with excellent properties in regeneration. Chemical Engineering Journal. 2017;230315:345–54.

9. Wang S, Peng Y. Natural zeolites as effective adsorbents in water and wastewater treatment. Vol. 156, Chemical Engineering Journal. 2010. p. 11–24. Available from: https://doi.org/10.1016/j.cej.2009.10.029

10. Martin BD, De Kock L, Gallot M, Guery E, Stanowski S, MacAdam J, et al. Quantifying the performance of a hybrid anion exchanger/adsorbent for phosphorus removal using mass spectrometry coupled with batch kinetic trials. Environmental Technology. 2018;39(18):2304–14. Available from: https://doi.org/10.1080/09593330.2017.1354076

11. Choi SS, Lee HM, Ha JH, Kang DG, Kim CS, Seo JH, et al. Biological removal of phosphate at low concentrations using recombinant Escherichia coli expressing phosphate-binding protein in periplasmic space. Appl Biochem Biotechnol. 2013 16;171(5):1170–7. Available from: http://link.springer.com/10.1007/s12010-013-0187-1

12. Hutchison J, Hussein F, Mayer B. Evaluating sustainable development pathways for protein- and peptide-based bioadsorbents for phosphorus recovery from wastewater. Environ Sci Technol. 2023; 57:16317-16326. Available from https://doi.org/10.1021/acs.est.3c04016

13. Hussein FB, Venkiteshwaran K, Mayer BK. Cell surface-expression of the phosphate-binding protein PstS: System development, characterization, and evaluation for phosphorus removal and recovery. J Environ Sci. 2020;92:129–40. Available from: https://doi.org/10.1016/j.jes.2020.02.016

14. Hussein FB, Mayer BK. Fixed-bed column study of phosphate adsorption using immobilized phosphate-binding protein. Chemosphere. 2022;295:133908. Available from: https://doi.org/10.1016/j.chemosphere.2022.133908

15. Li Q, Yu Z, Shao X, He J, Li L. Improved phosphate biosorption by bacterial surface display of phosphate-binding protein utilizing ice nucleation protein. FEMS Microbiol Lett. 2009;299(1):44–52. Available from: https://doi.org/10.1111/j.1574-6968.2009.01724.x

16. Venkiteshwaran K, Wells E, Mayer BK. Immobilized phosphate-binding protein can effectively discriminate against arsenate during phosphate adsorption and recovery. Water Environment Research. 2021;93(8):1173–8. Available from: https://doi.org/10.1002/wer.1498

17. Venkiteshwaran K, Wells E, Mayer BK. Kinetics, affinity, thermodynamics, and selectivity of phosphate removal using immobilized phosphate-binding proteins. Environ

Sci Technol. 2020;54(17):10885–94. Available from: https://doi.org/10.1021/acs.est.0c02272

18. Venkiteshwaran K, Pokhrel N, Hussein F, Antony E, Mayer BK. Phosphate removal and recovery using immobilized phosphate binding proteins. Water Res X. 2018;1:1–9. Available from: https://doi.org/10.1016/j.wroa.2018.09.003

19. Yang Y, Ballent W, Mayer BK. High-affinity phosphate-binding protein (PBP) for phosphorous recovery: Proof of concept using recombinant Escherichia coli. FEMS Microbiol Lett. 2016;363(20):1–6. Available from: https://doi.org/10.1093/femsle/fnw240

20. Gonçalves MB, Dreyer J, Lupieri P, Barrera-Patiño C, Ippoliti E, Webb MR, et al. Structural prediction of a rhodamine-based biosensor and comparison with biophysical data. Phys Chem Chem Phys. 2013;15(6):2177–83. Available from: https://doi.org/10.1039/C2CP42396K

21. Qi R, Jing Z, Liu C, Piquemal JP, Dalby KN, Ren P. Elucidating the phosphate binding mode of phosphate-binding protein: The critical effect of buffer solution. J Phys Chem B. 2018 Jun 21;122(24):6371–6. Available from: https://doi.org/10.1021/acs.jpcb.8b03194

22. Held M, Metzner P, Prinz JH, Noé F. Mechanisms of protein-ligand association and its modulation by protein mutations. Biophys J. 2011 Feb;100(3):701–10. Available from: https://doi.org/10.1016/j.bpj.2010.12.3699

23. Hutchison JM, Mayer BK, Vega M, Chacha WE, Zilles JL. Making Waves: Biocatalysis and biosorption: Opportunities and challenges associated with a new protein-based toolbox for water and wastewater treatment. Water Research X. 2021;12:100112. Available from: https://doi.org/10.1016/j.wroa.2021.100112

24. Vallabani NVS, Singh S. Recent advances and future prospects of iron oxide nanoparticles in biomedicine and diagnostics. 3 Biotech. 2018;8(6):1–23. Available from: http://dx.doi.org/10.1007/s13205-018-1286-z

25. Gómez-Pastora J, Bringas E, Ortiz I. Recent progress and future challenges on the use of high performance magnetic nano-adsorbents in environmental applications. Chemical Engineering Journal. 2014;256:187–204. Available from: https://doi.org/10.1016/j.cej.2014.06.119

26. APHA. Standard methods for the examination of water and wastewater. 21st ed. Washington, D.C.: American Public Health Association; 2005.

27. Wu L, Zhang S, Wang J, Ding X. Phosphorus retention using iron (II/III) modified biochar in saline-alkaline soils: Adsorption, column and field tests. Environmental Pollution. 2020;261:114223. Available from: https://doi.org/10.1016/j.envpol.2020.114223

28. Kuroda A, Kunimoto H, Morohoshi T, Ikeda T, Kato J, Takiguchi N, et al. Evaluation of phosphate removal from water by immobilized phosphate-binding protein PstS. J Biosci

Bioeng. 2000;90(6):688–90. Available from: https://doi.org/10.1016/S1389-1723(00)90020-3

29. Case DA, Ben-Shalom IY, Brozell SR, Cerutti DS, Cheatham TE, Cruzeiro IVWD, et al. AMBER 2019. University of California, San Francisco.; 2019. Available from: https://ambermd.org/doc12/Amber19.pdf

30. Hirshberg M, Henrick K, Lloyd Haire L, Vasisht N, Brune M, Corrie JET, et al. Crystal structure of phosphate binding protein labeled with a coumarin fluorophore, a probe for inorganic phosphate. Biochemistry. 1998 Jul 1;37(29):10381–5. Available from: https://doi.org/10.1021/bi980428z

31. Vanquelef E, Simon S, Marquant G, Garcia E, Klimerak G, Delepine JC, et al. R.E.D. Server: a web service for deriving RESP and ESP charges and building force field libraries for new molecules and molecular fragments. Nucleic Acids Res. 2011 Jul 1;39(suppl_2):W511–7. Available from: https://doi.org/10.1093/nar/gkr288

32. Tang T, Dong J, Ai S, Qiu Y, Han R. Electro-enzymatic degradation of chlorpyrifos by immobilized hemoglobin. J Hazard Mater. 2011;188(1–3):92–7. Available from: http://dx.doi.org/10.1016/j.jhazmat.2011.01.080

33. Jorgensen WL, Chandrasekhar J, Madura JD, Impey RW, Klein ML. Comparison of simple potential functions for simulating liquid water. J Chem Phys. 1983 Jul 15;79(2):926–35. Available from: https://doi.org/10.1063/1.445869

34. Joung IS, Cheatham TE. Determination of alkali and halide monovalent ion parameters for use in explicitly solvated biomolecular simulations. J Phys Chem B. 2008 Jul 1;112(30):9020–41. Available from: https://doi.org/10.1021/jp8001614

35. Umerani MJ, Pratakshya P, Chatterjee A, Cerna Sanchez JA, Kim HS, Ilc G, et al. Structure, self-assembly, and properties of a truncated reflectin variant. Proceedings of the National Academy of Sciences. 2020 Dec 29;117(52):32891–901. Available from: https://doi.org/10.1073/pnas.2009044117

36. Verma P, Kwansa AL, Ho R, Yingling YG, Zimmer J. Insights into substrate coordination and glycosyl transfer of poplar cellulose synthase-8. Structure. 2023 Oct;31(10):1166-1173.e6. Available from: https://doi.org/10.1016/j.str.2023.07.010

37. Roe DR, Cheatham TE. PTRAJ and CPPTRAJ: Software for processing and analysis of molecular dynamics trajectory data. J Chem Theory Comput. 2013 Jul 9;9(7):3084–95. Available from: https://doi.org/10.1021/ct400341p

38. Scheurer M, Rodenkirch P, Siggel M, Bernardi RC, Schulten K, Tajkhorshid E, et al. PyContact: Rapid, customizable, and visual analysis of noncovalent interactions in MD simulations. Biophys J. 2018 Feb;114(3):577–83. Available from: https://doi.org/10.1016/j.bpj.2017.12.003

39. Hubbe MA, Azizian S, Douven S. Implications of apparent pseudo-second-order adsorption kinetics onto cellulosic materials: A review. Bioresources.com. 2019;7582–627.

40. Tagliazucchi M, Szleifer I. How does confinement change ligand–receptor binding equilibrium? Protein binding in nanopores and nanochannels. J Am Chem Soc. 2015 Oct 7;137(39):12539–51. Available from: https://doi.org/10.1021/jacs.5b05032

41. López-Luna J, Ramírez-Montes LE, Martinez-Vargas S, Martínez AI, Mijangos-Ricardez OF, González-Chávez M del CA, et al. Linear and nonlinear kinetic and isotherm adsorption models for arsenic removal by manganese ferrite nanoparticles. SN Appl Sci. 2019;1(8):950. Available from: https://doi.org/10.1007/s42452-019-0977-3

42. Xu Q, Li W, Ma L, Cao D, Owens G, Chen Z. Simultaneous removal of ammonia and phosphate using green synthesized iron oxide nanoparticles dispersed onto zeolite. Science of the Total Environment. 2020;703:1–8. Available from: https://doi.org/10.1016/j.scitotenv.2019.135002

43. Mallet M, Barthélémy K, Ruby C, Renard A, Naille S. Investigation of phosphate adsorption onto ferrihydrite by X-ray photoelectron spectroscopy. J Colloid Interface Sci. 2013 Oct 1;407:95–101. Available from: https://doi.org/10.1016/j.jcis.2013.06.049

44. Kalaitzidou K, Zouboulis A, Mitrakas M. Thermodynamic study of phosphate adsorption and removal from water using iron oxyhydroxides. Water. 2022;14(1163):1–14.

45. Yousefi M, Nabizadeh R, Alimohammadi M, Mohammadi AA, Mahvi AH. Removal of phosphate from aqueous solutions using granular ferric hydroxide process optimization by response surface methodology. Desalination Water Treat. 2019;158:290–300. Available from: https://doi.org/10.5004/dwt.2019.24281

46. Do TH, Nguyen VT, Nguyen QD, Chu, Nhuong M, Ngo TCQ, Tan L Van. Equilibrium, kinetic and thermodynamic studies for sorption of phosphate from aqueous solutions using ZnO nanoparticles. Processes. 2020;8(1397):1–19. Available from: https://doi.org/10.1016/j.jtice.2018.07.034

47. Nandi BK, Goswami A, Purkait MK. Adsorption characteristics of brilliant green dye on kaolin. J Hazard Mater. 2009 Jan 15;161(1):387–95. Available from: https://doi.org/10.1016/j.jhazmat.2008.03.110

48. Ajmal Z, Muhmood A, Usman M, Kizito S, Lu J, Dong R, et al. Phosphate removal from aqueous solution using iron oxides: Adsorption, desorption and regeneration characteristics. J Colloid Interface Sci. 2018;528:145–55. Available from: https://doi.org/10.1016/j.jcis.2018.05.084

49. Luecke H, Quiocho F. High specificity of a phosphate transport protein determined by hydrogen bonds. Nature. 1990;347:402–6.

50. Sharafi Z, Bakhshi B, Javidi J, Adrangi S. Synthesis of silica-coated iron oxide nanoparticles: Preventing aggregation without using additives or seed pretreatment. Iranian Journal of Pharmaceutical Research. 2018;17(1):386–95.

51. Du X, Li Y, Xia YL, Ai SM, Liang J, Sang P, et al. Insights into protein–ligand interactions: Mechanisms, models, and methods. International Journal of Molecular Sciences. 2016;17:144. Available from: https://doi.org/10.3390/ijms17020144

52. Liu J, Wan L, Zhang L, Zhou Q. Effect of pH, ionic strength, and temperature on the phosphate adsorption onto lanthanum-doped activated carbon fiber. J Colloid Interface Sci. 2011 Dec 15;364(2):490–6. https://doi.org/10.1016/j.jcis.2011.08.067

53. Ledvina PS, Tsai AL, Wang Z, Koehl E, Quiocho FA. Dominant role of local dipolar interactions in phosphate binding to a receptor cleft with an electronegative charge surface: Equilibrium, kinetic, and crystallographic studies. Protein Science. 1998;7(12):2550–9. Available from: https://doi.org/10.1002/pro.5560071208

54. Wang Z, Choudhary A, Ledvina PS, Quiocho FA. Fine tuning the specificity of the periplasmic phosphate transport receptor. Site-directed mutagenesis, ligand binding, and crystallographic studies. J Biol Chem. 1994;269(40):25091–4.

55. Ayawei N, Ebelegi AN, Wankasi D. Modelling and interpretation of adsorption isotherms. Journal of Chemistry. 2017;3039817. Available from: https://doi.org/10.1155/2017/3039817

56. Mahanta N, Valiyaveetti S. Functionalized poly (vinyl alcohol) based nanofibers for the removal of arsenic from water. RSC Adv. 2013;3:2776–83.

57. Huang W, Yu X, Tang J, Zhu Y, Zhang Y, Li D. Enhanced adsorption of phosphate by flower-like mesoporous silica spheres loaded with lanthanum. Microporous and Mesoporous Materials. 2015;217:225–32. Available from: https://doi.org/10.1016/j.funbio.2012.12.004

58. Drenkova-Tuhtan A, Schneider M, Franzreb M, Meyer C, Gellermann C, Sextl G, et al. Pilot-scale removal and recovery of dissolved phosphate from secondary wastewater effluents with reusable ZnFeZr adsorbent @ Fe3O4/SiO2 particles with magnetic harvesting. Water Res. 2017;109:77–87. Available from: http://dx.doi.org/10.1016/j.watres.2016.11.039

59. Rashid M, Price NT, Gracia Pinilla MÁ, O'Shea KE. Effective removal of phosphate from aqueous solution using humic acid coated magnetite nanoparticles. Water Res. 2017;123:353–60. Available from: https://doi.org/10.1016/j.watres.2017.06.085

60. Suresh Kumar P, Prot T, Korving L, Keesman KJ, Dugulan I, van Loosdrecht MCM, et al. Effect of pore size distribution on iron oxide coated granular activated carbons for phosphate adsorption – Importance of mesopores. Chemical Engineering Journal. 2017;326:231–9. Available from: http://dx.doi.org/10.1016/j.cej.2017.05.147

61. Jubb HC, Higueruelo AP, Ochoa-Montaño B, Pitt WR, Ascher DB, Blundell TL. Arpeggio: A web server for calculating and visualising interatomic interactions in protein structures. J Mol Biol. 2017 Feb;429(3):365–71. Available from: https://doi.org/10.1016/j.jmb.2016.12.004

62. Salamanca Viloria J, Allega MF, Lambrughi M, Papaleo E. An optimal distance cutoff for contact-based protein structure networks using side-chain centers of mass. Sci Rep. 2017 Jun 6;7(1):2838. Available from: https://doi.org/10.1038/s41598-017-01498-6

63. Sobieraj M, Setny P. Entropy-based distance cutoff for protein internal contact networks. Proteins: Structure, Function, and Bioinformatics. 2021 Oct 10;89(10):1333–9. Available from: https://doi.org/10.1002/prot.26154

64. Cao L, Goreshnik I, Coventry B, Case JB, Miller L, Kozodoy L, et al. De novo design of picomolar SARS-CoV-2 miniprotein inhibitors. Science. 2020;370(6515):426–31. Available from: https://doi.org/10.1126/science.abd9909

65. Gupta S, Azadvari N, Hosseinzadeh P. Design of protein segments and peptides for binding to protein targets. BioDesign Research. 2022 Jan 16;2022. Available from: https://doi.org/10.34133/2022/9783197

66. Tsai CY, Salawu EO, Li H, Lin GY, Kuo TY, Voon L, et al. Helical structure motifs made searchable for functional peptide design. Nat Commun. 2022 Jan 10;13(1):102. Available from: https://doi.org/10.1038/s41467-021-27655-0

67. Fowler WC, Deng C, Griffen GM, Teodoro OT, Guo AZ, Zaiden M, et al. Harnessing peptide binding to capture and reclaim phosphate. J Am Chem Soc. 2021 24;143(11):4440–50. Available from: https://doi.org/10.1021/jacs.1c01241